

Acoustic vibrations of anisotropic nanoparticles

Lucien Saviot^{1,*} and Daniel B. Murray^{2,†}

¹*Institut Carnot de Bourgogne, UMR 5209, CNRS-Université de Bourgogne, 9 Avenue A. Savary, BP 47870, F-21078 Dijon Cedex, France*

²*Mathematics, Statistics, and Physics Unit, The University of British Columbia Okanagan, 3333 University Way, Kelowna, British Columbia, Canada V1V1V7*

(Received 17 February 2009; revised manuscript received 20 April 2009; published 1 June 2009)

Acoustic vibrations of nanoparticles made of materials with anisotropic elasticity and nanoparticles with nonspherical shapes are theoretically investigated using a homogeneous continuum model. Cubic, hexagonal, and tetragonal symmetries of the elasticity are discussed, as are spheroidal, cuboctahedral, and truncated cuboctahedral shapes. Tools are described to classify the different vibrations and, for example, help identify the modes having a significant low-frequency Raman-scattering cross section. Continuous evolutions of the modes starting from those of an isotropic sphere coupled with the determination of the irreducible representation of the branches permit some qualitative statements to be made about the nature of various modes. For spherical nanoparticles, a more accurate picture is obtained through projections onto the vibrations of an isotropic sphere.

DOI: [10.1103/PhysRevB.79.214101](https://doi.org/10.1103/PhysRevB.79.214101)

PACS number(s): 63.22.Kn

I. INTRODUCTION

The lowest-frequency vibrations of isolated nanoparticles are in the THz range, on the order of the speed of sound divided by the dimension. These are commonly referred to as confined acoustic phonons and are unrelated to optical phonons. There have been numerous experimental and theoretical studies on the acoustic vibrations of nanoparticles in the last few decades. These vibrations have been observed by a variety of experimental techniques including low-frequency Raman scattering,¹ time-resolved femtosecond pump-probe experiments,²⁻⁴ infrared absorption,^{5,6} inelastic neutron scattering,⁷ and persistent spectral hole burning.³

Reasonable estimates for the mode frequencies are obtained using the 1882 Lamb solution of the continuum elastic problem for an elastically isotropic homogeneous free sphere.⁸ This provided sufficiently good agreement to confirm that confined acoustic phonon modes were really being observed. However, this model was unable to deal with the anisotropy of actual samples.

Recent advances have permitted the creation of high quality elastically anisotropic samples.⁹ The essential features are (1) a narrow size distribution, (2) good crystallinity so that a significant amount of nanoparticles in the sample are monodomain, (3) controlled shape of nanoparticles, and (4) separation of nanoparticles so that they vibrate as independent units. As a result, the vibrational modes of elastically anisotropic nanoparticles have been observed. This has created the need for an alternative to the Lamb model capable of dealing with nanoparticles with lower symmetry.

In this work, we use the method of Visscher *et al.*¹⁰ which is a standard numerical approach suitable for the calculation of the frequencies and the wave functions of the vibrations of such nanoparticles. The symmetry of these modes, their volume variation, and their Lamb mode parentage are determined and applied to the prediction of their observation by different experimental techniques such as inelastic light scattering.

II. METHODS

The situation for an isotropic nanoparticle will now be summarized. In this case, the system is spherically symmetric. Thus, vibrational modes can be classified by their angular momentum number $\ell \geq 0$ and its z component m . Modes can also be classified either as torsional (T) or spheroidal (S). Finally, modes are also indexed in order of frequency by $n \geq 1$ [$n=1$ corresponds to the first harmonic (fundamental mode), $n=2$ to the second harmonic and so on]. In the following, we will indicate Lamb modes using the compact notation $X_{\ell m}^n$ where $X=S$ or $X=T$.

All modes can be observed by inelastic neutron scattering in the typical situation where the wavelength of the neutrons is much smaller than the nanoparticle size. For nanoparticles whose dimension is small compared to the wavelength of light (dipolar approximation), Raman only detects S_0 and S_2 , infrared absorption only detects S_1 (Ref. 11) and time-resolved femtosecond pump-probe experiments typically only detect S_0 . In the following, we will assume that the nanoparticles are small enough so that the dipolar approximation holds.

Nanoparticles with either isotropic or anisotropic elasticity will be considered in the following. Isotropic elasticity is considered mainly for comparison with previous studies. Anisotropic elasticity is used for perfect nanocrystals consisting of a single domain. We will refer to such nanoparticles as being “monodomain” in the following. In a small nanoparticle, a monodomain structure is not necessarily energetically favorable. For example, it is well known that multiply-twinned silver nanoparticles are much more stable for certain ranges of size.¹²

A. Calculation of frequencies and associated displacements

The frequencies and their associated displacements for an anisotropic nanoparticle have been calculated using the approach introduced by Visscher *et al.*¹⁰ which also assumes continuum elasticity. Other authors have already confirmed

TABLE I. Degeneracy lifting of spheroidal Lamb modes with $\ell \leq 4$ for various symmetries. The degeneracy lifting for torsional modes (with $\ell > 0$) is obtained by changing the parities ($u \leftrightarrow g$).

Point group	S_0	S_1	S_2	S_3	S_4
O_h	A_{1g}	T_{1u}	$E_g + T_{2g}$	$A_{2u} + T_{1u} + T_{2u}$	$A_{1g} + E_g + T_{1g} + T_{2g}$
D_{4h}	A_{1g}	$A_{2u} + E_u$	$A_{1g} + B_{1g} + B_{2g} + E_g$	$A_{2u} + B_{1u} + B_{2u} + 2E_u$	$2A_{1g} + A_{2g} + B_{1g} + B_{2g} + 2E_g$
D_{6h}	A_{1g}	$A_{2u} + E_{1u}$	$A_{1g} + E_{1g} + E_{2g}$	$A_{2u} + B_{1u} + B_{2u} + E_{1u} + E_{2u}$	$A_{1g} + B_{1g} + B_{2g} + E_{1g} + 2E_{2g}$
$D_{\infty h}$	A_{1g}	$A_{1u} + E_{1u}$	$A_{1g} + E_{1g} + E_{2g}$	$A_{1u} + E_{1u} + E_{2u} + E_{3u}$	$A_{1g} + E_{1g} + E_{2g} + E_{3g} + E_{4g}$

that the convergence of this method is faster than the convergence of finite element methods at least in some cases.¹³ The relevance of continuum elasticity for nanoparticles has been confirmed using atomistic calculations^{14–17} for nanoparticles larger than 2–3 nm and even for ZnO nanoparticles for which surface relaxation and stress are significant.¹⁸ Most of the results presented in this paper have been obtained for nanospheres whose diameter is 10 nm which is well above these limits. It is possible to extrapolate them to different sizes since the frequencies vary as the inverse diameter. However care should be taken not to consider very small nanoparticles for which surface effects could significantly alter the validity of the continuum approximation. The calculational method for the modes gives each mode in terms of power-series coefficients a_{ijpqr} so that

$$\vec{u}_i(x, y, z) = \sum_{pqr} \sum_{j=x, y, z} a_{ijpqr} x^p y^q z^r \vec{j}. \quad (1)$$

The power expansion covered $0 \leq p+q+r \leq 20$ for good convergence for all the modes we are interested in. The frequencies for the isotropic spherical case were reproduced with very good accuracy. The convergence for strongly anisotropic systems is harder to check. Despite checking that the frequencies do not significantly change when adding more terms to the power expansion, we also compared the calculated frequencies with the finite element mesh sequence (FEMS) method introduced in a previous work.¹⁹

In this work, all the displacements have been normalized according to Eq. (2), where V is the volume of the nanoparticle,²⁰

$$\iiint_V \vec{u}_i \cdot \vec{u}_j d^3\vec{R} = V \delta_{ij}. \quad (2)$$

B. Group theory

1. Degeneracy lifting

In the absence of spherical symmetry, modes are classified according to their remaining symmetry. For example, for a spherical nanoparticle with cubic elasticity, such as Ag, Au, and Si, the system is symmetric under the symmetry operations of a cube, which is the 48-element group O_h .

Our calculations return a large number of modes which have to be considered to interpret inelastic light-scattering spectra or other experimental results. It is important to use not only the frequencies but also the wave functions in order to do that. Group theory is a very valuable tool in this con-

text as it allows, for example, to identify the Raman-active modes and therefore simplify the assignment process. In this work, we will only consider nanoparticles whose dimensions are small compared to the wavelength of light (dipolar approximation) in order to discuss the selection rules of Raman scattering. Table I shows how the degeneracy of the Raman and infrared-active modes of an isotropic sphere¹¹ is lifted or not when lowering the symmetry. Only point groups relevant for the rest of this paper are considered.

2. Numerical determination of the irreducible representations

In order to take full advantage of group theory, it is important to label the different modes with the corresponding irreducible representation. Sophisticated and specific approaches could be considered to restrict the calculations to modes having a well-defined symmetry. However, we preferred to keep the numerical approach detailed previously because it is more general. We added a few calculation steps to determine the irreducible representation from the wave functions. It turns out this can be achieved very reliably and without much additional calculation time.

S being a symmetry operation of the point group of concern and u_i with $i=1, \dots, n$ a full set of eigenmodes having the same frequency, the character of S for this irreducible group of vibrations is

$$\xi(S) = \sum_{i=1}^n \int \int \int_V S[\vec{u}_i(\vec{R})] \cdot \vec{u}_i[S(\vec{R})] d^3\vec{R}. \quad (3)$$

Such integrals can be calculated accurately and quickly when each Cartesian component of the displacement field is a sum of terms of the form $x^p y^q z^r$. By calculating a few well-chosen characters, it is then straightforward to distinguish all the different irreducible representations using the character table of the point group. The only restriction to applying this procedure is that the degeneracy must be known and therefore the convergence must be good. Of course, a more general approach is required to handle accidental degeneracies.

In the following we detail some additional ways to improve our knowledge of these vibrations. These are needed since regarding Raman scattering many modes are labeled as Raman active due to the irreducible representation they belong to. However there is not necessarily an efficient coupling mechanism enabling a significant Raman intensity. The following tools are designed to somewhat address this problem.

C. Volume variation

The volume of the nanoparticle does not change for every possible vibration. For isotropic spherical nanoparticles, the volume changes only for the spheroidal $\ell=0$ vibration. This volume change is also involved in the time-resolved femto-second pump-probe measurements.² As a result, it is interesting to calculate it for all the vibrations.

The volume variation corresponds to the flux of the displacement through the surface of the particle. The expression for a dimensionless volume variation δV is given in Eq. (4). Using the divergence theorem, this two-dimensional (2D) integral can be turned into a volume integral involving derivatives of $x^p y^q z^r$ functions which are already calculated in the frame of Visscher's method.¹⁰ Therefore this quantity can also be accurately and efficiently calculated. It can be shown that the volume variation is different from zero for fully symmetric vibrations only, i.e., for A_{1g} vibrations for the symmetries considered here,

$$\delta V_i V^{2/3} = \left| \iint_S \vec{u}_i(\vec{R}) \cdot d\vec{S} \right| = \left| \iiint_V \text{div}[\vec{u}_i(\vec{R})] d^3\vec{R} \right|. \quad (4)$$

Of course, the value of δV depends on the normalization [see Eq. (2)].

D. Smooth variation of parameters

In order to follow how the vibrations evolve when lowering the symmetry, it is possible to follow the frequencies of the different modes while slowly varying the parameters (for example, the shape or the elastic constants of the material the nanoparticle is made of). The curve representing the variation in one frequency is called a branch in the following. Group theory can help plotting such branches more reliably because all the different points on a given branch share the same irreducible representation. Moreover branches having different irreducible representations can cross but not branches having the same irreducible representation. This originates from the coupling between the different branches being due to the anisotropy itself whose irreducible representation is A_{1g} for the point groups we focus on. As a result, all n th modes having a given irreducible representation belong to the same branch and can be safely connected.

In this work, branches due to varying elastic anisotropy are calculated by changing the stiffness tensor using $C(x) = (1-x)C^{\text{iso}} + xC^{\text{ani}}$, with $0 \leq x \leq 1$, C^{iso} being the tensor of the isotropic material (which can be obtained by averaging the sound velocities¹⁹ or other methods²¹ or using measured longitudinal and transverse sound velocities), and C^{ani} the anisotropic tensor. The parameters used in this work are given in Ref. 22. It should be noted that such branches are made of fictive materials except for $x=1$ where the real elastic parameters of the bulk material are used.

E. Projections

When the lowering of the symmetry is not due to a change in the shape of the nanoparticle, it is possible to

TABLE II. Characteristics of the modes of a monodomain Ag sphere with $R=5$ nm are shown. i is the mode index. The two largest projections onto Lamb modes are shown.

i	ν (GHz)	ir	Squared Lamb projections	δV
7–8	103.3	E_g	$0.995S_2^1 + 0.002S_4^1 + \dots$	0.0
9–11	106.8	T_{2u}	$0.936T_2^1 + 0.054S_3^1 + \dots$	0.0
12	151.1	A_{2g}	$0.996T_3^1 + 0.002S_6^1 + \dots$	0.0
13–15	153.0	T_{1u}	$0.499S_3^1 + 0.480S_1^1 + \dots$	0.0
16–17	161.0	E_u	$0.974T_2^1 + 0.018T_4^1 + \dots$	0.0
18–20	169.4	T_{2g}	$0.821S_2^1 + 0.160T_3^1 + \dots$	0.0
21–23	196.4	T_{2g}	$0.758T_3^1 + 0.178S_2^1 + \dots$	0.0
24–26	196.9	T_{1g}	$0.411T_3^1 + 0.369S_4^1 + \dots$	0.0
27–28	211.2	E_g	$0.838S_2^1 + 0.113S_4^1 + \dots$	0.0
29–31	221.8	T_{2u}	$0.748T_4^1 + 0.199S_3^1 + \dots$	0.0
32–34	232.1	T_{1u}	$0.466S_3^1 + 0.466S_1^1 + \dots$	0.0
35–37	234.5	T_{2u}	$0.665S_3^1 + 0.127T_4^1 + \dots$	0.0
38	248.9	A_{1g}	$0.959S_4^1 + 0.028S_0^1 + \dots$	0.4
...
75	331.2	A_{1g}	$0.930S_0^1 + 0.039S_4^2 + \dots$	4.3
...

compare the wave functions (omitting their time dependences) of the two systems. As commonly done for atomistic calculations,^{14–16} we calculated the projection of the displacements of spherical nanoparticles onto Lamb modes. For a given mode whose displacement is $\vec{u}_i(\vec{R})$ the projection onto the Lamb mode $\vec{X}_{\ell m}^n$ is defined as

$$P(u_i, X_{\ell m}^n) = \frac{1}{V} \iiint_V \vec{u}_i(\vec{R}) \cdot \vec{X}_{\ell m}^n(\vec{R}) d^3\vec{R}. \quad (5)$$

The orthonormality and completeness of the Lamb modes implies that for any i ,

$$\sum_{\ell} \sum_m \sum_n P(u_i, X_{\ell m}^n)^2 = 1. \quad (6)$$

Likewise, the orthonormality and completeness of the modes of the anisotropic nanoparticle implies that for any ℓ , m , and n ,

$$\sum_i P(u_i, X_{\ell m}^n)^2 = 1. \quad (7)$$

However, a more relevant quantity is obtained by summing the squared projections over all the degenerate Lamb modes, i.e., over m . As a result, the total squared projection of u_i onto the subspace spanned by the $2\ell + 1$ modes X_{ℓ}^n is

$$\sum_{m=-\ell}^{\ell} P(u_i, X_{\ell m}^n)^2. \quad (8)$$

The Lamb projections given in the fourth columns of Tables II–VII correspond to this last quantity. It represents the ratio of the energy contained in the projection onto Lamb mode X_{ℓ}^n to that of mode i assuming the same frequencies.

TABLE III. Characteristics of the modes of a monodomain sphere of Au with $R=5$ nm. i is the mode index. The two largest projections onto the Lamb modes are shown.

i	ν (GHz)	ir	Squared Lamb projections	δV
7–8	74.6	E_g	$0.996S_2^1+0.002S_4^1+\dots$	0.0
9–11	76.9	T_{2u}	$0.939T_2^1+0.053S_3^1+\dots$	0.0
12	109.0	A_{2g}	$0.996T_3^1+0.002S_6^1+\dots$	0.0
13–15	111.2	T_{1u}	$0.516S_3^1+0.466S_1^1+\dots$	0.0
16–17	114.1	E_u	$0.977T_2^1+0.016T_4^1+\dots$	0.0
18–20	120.5	T_{2g}	$0.837S_2^1+0.146T_3^1+\dots$	0.0
21–23	140.2	T_{2g}	$0.773T_3^1+0.162S_2^1+\dots$	0.0
24–26	141.8	T_{1g}	$0.433T_3^1+0.356S_4^1+\dots$	0.0
27–28	154.0	E_g	$0.824S_2^2+0.126S_4^1+\dots$	0.0
29–31	158.9	T_{2u}	$0.698T_4^1+0.259S_3^1+\dots$	0.0
32–34	168.2	T_{2u}	$0.617S_3^1+0.186T_4^1+\dots$	0.0
35–37	169.7	T_{1u}	$0.484S_1^1+0.456S_3^1+\dots$	0.0
...
43	182.0	A_{1g}	$0.987S_4^1+0.005S_0^1+\dots$	0.1
...
118	285.8	A_{1g}	$0.594S_4^2+0.218S_8^1+\dots$	1.2
...
133	301.9	A_{1g}	$0.866S_6^1+0.049S_8^1+\dots$	0.3
...
141	310.1	A_{1g}	$0.806S_0^1+0.133S_8^1+\dots$	3.9
...
183	341.5	A_{1g}	$0.378S_8^1+0.319S_4^2+\dots$	1.4
...

III. APPLICATIONS

A. Spherical nanocrystals with cubic crystallinity

1. Spherical monodomain silver and gold nanoparticles

Let us first consider the case of a spherical nanoparticle made of silver. This nanoparticle is monodomain, and therefore the stiffness tensor is the same everywhere inside the nanoparticle and identical to that of bulk silver.²³ Table II presents the calculated frequencies, irreducible representations, main projections onto the modes of an isotropic silver sphere, and volume variations in the lowest-frequency modes. The six modes $i=1-6$ have zero frequency and correspond to the rigid rotations and translations of the nanoparticle. The branches corresponding to the lowering of the symmetry when going from the isotropic to the anisotropic case are plotted in Fig. 1.

Figure 1 clearly shows that the introduction of elastic anisotropy significantly lifts the degeneracy of most modes. One notable exception is the breathing mode which corresponds to the second A_{1g} branch. This mode is nondegenerate, and its frequency hardly changes with anisotropy. The other important exceptions are the dipolar modes S_1 which are infrared active and transform into T_{1u} with the same degeneracy. The lowest Raman-active mode S_2^1 which has de-

TABLE IV. Characteristics of the modes of a monodomain anatase TiO_2 sphere with $R=5$ nm are shown. i is the mode index. The two largest projections onto Lamb modes are shown.

i	ν (GHz)	ir	Squared Lamb projections	δV
7	283.5	A_{1g}	$0.977S_2^1+0.016S_0^1+\dots$	0.6
8–9	284.0	E_u	$0.931T_2^1+0.054S_1^1+\dots$	0.0
10	298.5	A_{1u}	$0.999T_2^1+0.000T_9^1+\dots$	0.0
11	304.3	B_{1u}	$0.998T_2^1+0.001S_3^1+\dots$	0.0
12–13	316.1	E_g	$0.996S_2^1+0.002T_3^1+\dots$	0.0
14	326.9	B_{2g}	$0.992S_2^1+0.008T_3^1+\dots$	0.0
15	330.9	B_{2u}	$0.967T_2^1+0.027S_3^1+\dots$	0.0
16	381.5	B_{1g}	$0.965S_2^1+0.033T_3^1+\dots$	0.0
17	432.4	A_{2u}	$0.494S_1^1+0.436S_3^1+\dots$	0.0
18	443.3	B_{2g}	$0.950T_3^1+0.028S_2^2+\dots$	0.0
19–20	445.7	E_u	$0.612S_1^1+0.323S_3^1+\dots$	0.0
21	447.6	A_{2u}	$0.537S_3^1+0.448S_1^1+\dots$	0.0
22–23	455.5	E_g	$0.957T_3^1+0.015S_4^1+\dots$	0.0
24–25	463.4	E_u	$0.758S_3^1+0.220S_1^1+\dots$	0.0
26	470.7	A_{2g}	$0.989T_3^1+0.005T_1^1+\dots$	0.0
27	473.9	B_{1g}	$0.865T_3^1+0.060S_4^1+\dots$	0.0
28	476.9	B_{1u}	$0.987S_3^1+0.008T_4^1+\dots$	0.0
29–30	480.7	E_g	$0.941T_3^1+0.031S_4^1+\dots$	0.0
31	510.9	B_{2u}	$0.946S_3^1+0.026T_4^1+\dots$	0.0
32–33	537.1	E_u	$0.826S_3^1+0.095S_1^1+\dots$	0.0
34	573.8	A_{1g}	$0.974S_4^1+0.009S_4^2+\dots$	0.0
35	580.8	A_{1g}	$0.910S_2^2+0.030S_2^3+\dots$	0.8
...
55	678.4	A_{1g}	$0.885S_4^1+0.082T_5^1+\dots$	0.2
...
67	743.1	A_{1g}	$0.803S_0^1+0.156T_5^1+\dots$	4.0
...
69	751.6	A_{1g}	$0.675T_5^1+0.162S_0^1+\dots$	1.8
...

generacy 5 is split into the lowest E_g and T_{2g} branches ($i=7, 8$ and $i=18-20$ in Table II, respectively) as expected from Table I. These anisotropic modes have a dominant projection onto S_2^1 confirming their Lamb mode parentage.

Similar calculations have been performed for monodomain gold nanoparticles using the elastic constants from Ref. 24, and the results are presented in Table III and Fig. 2. Compared to the previous case of silver, only the values of the stiffness tensor were changed so most observations previously made still apply. We recently reported on the experimental observation of the splitting of S_2^1 for such nanoparticles.⁹ There is an excellent agreement between these measurements and the splitting calculated using the present approach. This strongly supports the validity of our approach and in particular the relevance of elastic anisotropy even in such very small nanoparticles.

One notable difference between gold and silver concerns the case of the breathing mode. The isotropic breathing mode at 311.6 GHz belongs to the third A_{1g} branch. Therefore it is

TABLE V. Characteristics of the modes of a monodomain rutile TiO_2 sphere with $R=5$ nm are shown. i is the mode index. The two largest projections onto Lamb modes are shown.

i	ν (GHz)	ir	Squared Lamb projections	δV
7	288.1	B_{1g}	$0.978S_2^1+0.013T_3^1+\dots$	0.0
8	296.9	B_{2u}	$0.943T_2^1+0.045S_3^1+\dots$	0.0
9–10	355.8	E_u	$0.693T_2^1+0.150S_3^1+\dots$	0.0
11	419.8	A_{1u}	$0.981T_2^1+0.013T_4^1+\dots$	0.0
12–13	444.1	E_g	$0.927S_2^1+0.062T_3^1+\dots$	0.0
14	453.1	A_{1g}	$0.955S_2^1+0.035S_0^1+\dots$	0.8
15	481.0	B_{1u}	$0.965T_2^1+0.033S_3^1+\dots$	0.0
16	499.4	B_{1g}	$0.715T_3^1+0.210S_2^2+\dots$	0.0
17–18	531.7	E_u	$0.402S_1^1+0.288T_2^1+\dots$	0.0
19–20	537.1	E_g	$0.813T_3^1+0.071S_2^1+\dots$	0.0
21	539.4	A_{2g}	$0.465T_3^1+0.327S_4^1+\dots$	0.0
22	555.0	B_{2g}	$0.997S_2^1+0.001S_4^1+\dots$	0.0
23	558.9	A_{2u}	$0.969S_1^1+0.016S_3^1+\dots$	0.0
24	600.0	B_{2u}	$0.845S_3^1+0.095T_4^1+\dots$	0.0
25–26	622.3	E_u	$0.575S_3^1+0.247S_1^1+\dots$	0.0
...
38	744.0	A_{1g}	$0.739S_4^1+0.157S_0^1+\dots$	1.4
39–40	744.2	E_u	$0.725S_3^1+0.178S_1^1+\dots$	0.0
41	775.8	A_{1g}	$0.631S_0^1+0.269S_2^2+\dots$	4.1
...
50	836.1	A_{1g}	$0.439S_2^2+0.351S_4^1+\dots$	1.6
...
62	911.0	A_{1g}	$0.739S_4^1+0.169S_2^2+\dots$	0.9
...
81	1019.1	A_{1g}	$0.649T_5^1+0.110S_6^1+\dots$	0.5
...

tempting to assume that the anisotropic breathing mode lies on the same branch and is therefore mode $i=133$ at 301.9 GHz. However, Table III reveals that mode $i=141$ is a much better candidate for a breathing mode due to its larger volume variation and projection onto S_0^1 . It turns out this is due to a strong mixing of the A_{1g} branches as anisotropy is increased. Indeed, the isotropic modes S_4 , S_6 , and S_8 are split into various irreducible representations, one of them being A_{1g} . Unlike the previous case of silver, the elastic constants of gold result in four A_{1g} branches coming from S_0^1 , S_4^2 , S_6^1 , and S_8^1 being in the same frequency range. As a result, mode $i=141$ which is the mode having the strongest projection onto S_0^1 and also has a large volume variation does not lie on the same branch as S_0^1 . Figure 3 shows the variation in the squared projections onto S_0^1 of three of these A_{1g} branches as the elastic anisotropy is varied and confirms the mixing discussed above.

Similar but less pronounced mixings are observed in all cases. The density of modes (i.e., the number of modes per unit frequency) increases with frequency. As a result, the probability of mixings increases with frequency or i . This explains why the lowest-frequency modes such as the lowest

TABLE VI. Characteristics of the modes of a monodomain wurtzite CdSe sphere with $R=5$ nm are shown. i is the mode index. The two largest projections onto Lamb modes are shown.

i	ν (GHz)	ir	Squared Lamb projections	δV
7	119.4	A_{1u}	$1.000T_2^1+0.000T_8^1+\dots$	0.0
8–9	123.2	E_{2u}	$0.998T_2^1+0.001S_3^1+\dots$	0.0
10–11	126.8	E_{1g}	$0.999S_2^1+0.001T_3^1+\dots$	0.0
12–13	132.6	E_{2g}	$0.998S_2^1+0.002T_3^1+\dots$	0.0
14–15	132.8	E_{1u}	$0.971T_2^1+0.023S_3^1+\dots$	0.0
16	158.6	A_{1g}	$0.999S_2^1+0.001S_4^1+\dots$	0.0
17–18	181.3	E_{1u}	$0.894S_1^1+0.103S_3^1+\dots$	0.0
19	181.9	A_{2u}	$0.789S_1^1+0.206S_3^1+\dots$	0.0
20	186.1	A_{2g}	$0.999T_3^1+0.001T_1^1+\dots$	0.0
21–22	189.2	$B_{1g}+B_{2g}$	$0.994T_3^1+0.004S_4^1+\dots$	0.0
23–24	192.1	E_{2u}	$0.998S_3^1+0.001T_2^1+\dots$	0.0
25–26	193.5	E_{1g}	$0.980T_3^1+0.014S_4^1+\dots$	0.0
27–28	198.1	$B_{1u}+B_{2u}$	$0.996S_3^1+0.004T_4^1+\dots$	0.0
29–30	208.0	E_{2g}	$0.947T_3^1+0.042S_4^1+\dots$	0.0
31–32	214.7	E_{1u}	$0.870S_3^1+0.099S_1^1+\dots$	0.0
33	226.7	A_{2u}	$0.789S_3^1+0.206S_1^1+\dots$	0.0
...
55	273.8	A_{1g}	$0.926S_4^1+0.060S_2^2+\dots$	0.3
56	284.9	A_{2g}	$0.999T_1^1+0.001T_3^1+\dots$	0.0
57	296.0	A_{1g}	$0.925S_2^2+0.059S_4^1+\dots$	0.2
...
77	320.4	A_{1g}	$0.985S_0^1+0.011S_4^1+\dots$	4.5
...

E_g ones are almost pure isotropic modes (S_2^1). However, the lowest T_{2g} branches which are issued from the same S_2^1 and from T_3^1 are already significantly mixed by anisotropy for both gold and silver nanoparticles. This is clearly evidenced in Fig. 3 too.

TABLE VII. Characteristics of the modes of a monodomain Co sphere with $R=5$ nm are shown. i is the mode index. The two largest projections onto Lamb modes are shown.

i	ν (GHz)	ir	Squared Lamb projections	δV
7–8	229.8	E_{2u}	$0.998T_2^1+0.001T_4^1+\dots$	0.0
9	232.2	A_{1u}	$1.000T_2^1+0.000T_8^1+\dots$	0.0
10–11	240.7	E_{2g}	$0.997S_2^1+0.003T_3^1+\dots$	0.0
12–13	246.6	E_{1g}	$1.000S_2^1+0.000T_8^1+\dots$	0.0
14–15	251.4	E_{1u}	$0.942T_2^1+0.029S_1^1+\dots$	0.0
16	316.1	A_{1g}	$0.996S_2^1+0.003S_2^2+\dots$	0.0
17–18	334.7	E_{1u}	$0.919S_1^1+0.063S_3^1+\dots$	0.0
19	346.4	A_{2u}	$0.828S_1^1+0.167S_3^1+\dots$	0.0
...
49	497.8	A_{1g}	$0.958S_0^1+0.042S_4^1+\dots$	4.5
...

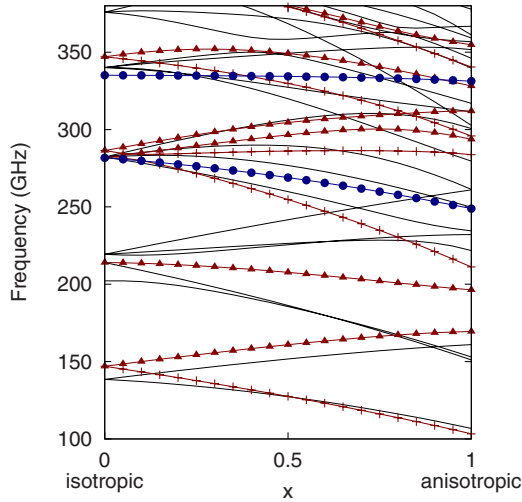


FIG. 1. (Color online) Evolution of the frequency of Raman-active modes of a monodomain silver sphere (radius 5 nm) with varying elastic anisotropy up to the frequency range of the breathing mode. Raman-inactive modes are plotted with black lines, E_g branches with lines and crosses (red online), T_{2g} branches with lines and triangles (red online), and A_{1g} branches with lines and full circles (blue online).

2. Raman-scattering efficiency for metallic cubic materials

Low-frequency Raman scattering from silver and gold nanoparticles has attracted a lot of attention during the last few decades. The scattering mechanisms have been identified²⁵ and one might wonder how the anisotropic considerations detailed in this work fit into this picture. The inelastic light-scattering process for such nanoparticles is mediated by the dipolar plasmon. As a result only scattering by S_0 and S_2 modes is allowed¹¹ and has a significant

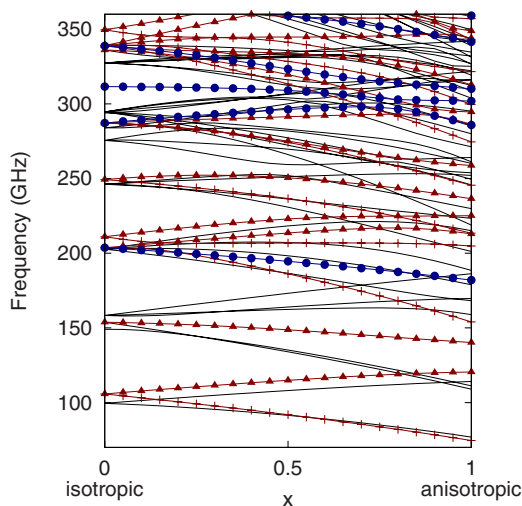


FIG. 2. (Color online) Evolution of the frequency of Raman-active modes of a monodomain gold sphere (radius 5 nm) with varying elastic anisotropy up to the frequency range of the breathing mode. Raman-inactive modes are plotted with black lines, E_g branches with lines and crosses (red online), T_{2g} branches with lines and triangles (red online), and A_{1g} branches with lines and full circles (blue online).

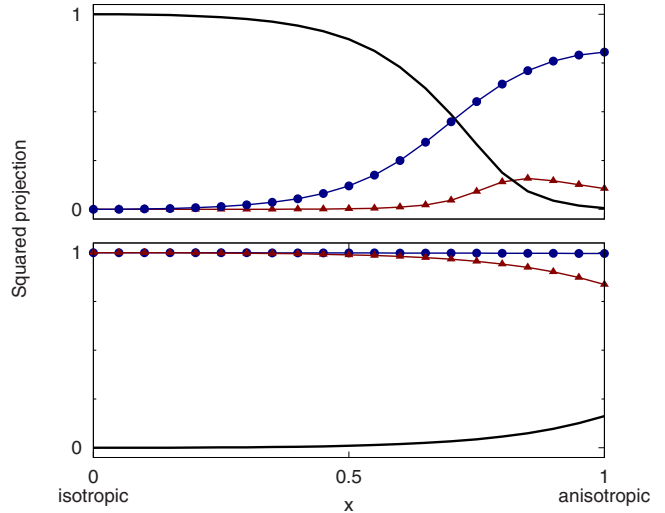


FIG. 3. (Color online) Evolution of the squared projection of several modes of a monodomain gold sphere (radius 5 nm) with varying elastic anisotropy. The bottom plot shows the squared projections onto S_2^1 of the E_g branch coming from S_2^1 (line with circles, blue online) and the T_{2g} branches coming from S_2^1 (line with triangles, red online) and T_3^1 (black line). The upper plot shows the squared projections onto S_0^1 of the A_{1g} branches coming from S_6^1 (line and triangles, red online), S_0^1 (black line), and S_4^2 (line and circles, blue online).

Raman-scattering cross section²⁵ in the isotropic case. Anisotropic nanoparticles obey the same rules and one might qualitatively estimate their Raman intensity by using the projections onto the same isotropic modes. As a result a significant scattering intensity is expected for the lowest E_g and T_{2g} modes of both silver and gold, while the second T_{2g} mode should have a small Raman cross section due to its small projection onto S_2^1 . The volume mechanism enables a measurable Raman intensity for the A_{1g} modes having a significant projection onto S_0 , i.e., for modes $i=75$ and $i=141$ for silver and gold, respectively. The Raman intensity for other A_{1g} modes should be very weak and probably not measurable in practice.

3. Other cubic materials

For cubic materials, the degree of elastic anisotropy is quantified by the Zener anisotropy ratio, $A=2C_{44}/(C_{11}-C_{12})$. $A=1$ for an isotropic material. Silver and gold both have $A \approx 3$ and also had the largest mode splittings that we found. For comparison, we mention results for some less anisotropic materials. For a silicon nanosphere with radius 5 nm, the Lamb mode S_2^1 splits into two frequencies at 386.6 GHz (E_g) and 485.9 GHz (T_{2g}). For a germanium nanosphere, the same mode is split into 235.1 GHz (E_g) and 295.3 GHz (T_{2g}). Using the standard deviation as a simple measure of the frequency splitting Δ (and therefore neglecting the effect of mixings), we obtain $\Delta=23\%$, 22% , 10% , and 11% for Ag, Au, Si, and Ge, respectively. For all these commonly studied materials, this splitting cannot be neglected.

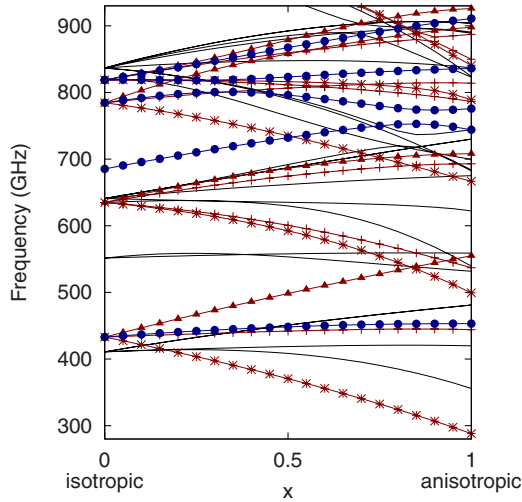


FIG. 4. (Color online) Evolution of the frequency of Raman-active modes of a monodomain rutile TiO_2 sphere (radius 5 nm) with varying elastic anisotropy up to the frequency range of the breathing mode. Raman-inactive modes are plotted with black lines, E_g branches with lines and crosses (red online), B_{1g} branches with lines and asterisks (red online), B_{2g} branches with lines and triangles (red online), and A_{1g} branches with lines and full circles (blue online).

B. Spherical nanocrystals with tetragonal crystallinity

Nanospheres with tetragonal crystallinity have a lower symmetry than the previous nanospheres with cubic crystallinity. The corresponding point group is D_{4h} . As a result, more degeneracy lifting occurs. This results in a splitting of the infrared-active S_1 mode into A_{2u} and E_u and four branches starting from the S_2^1 mode (A_{1g} , B_{1g} , B_{2g} , and E_g). The relative order of these branches depends on the stiffness tensor. Two nanospheres made of TiO_2 with radius 5 nm will be considered using the parameters from Ref. 26. One of them has the anatase crystal structure (Table IV) and the other the rutile structure (Table V and Fig. 4). We used these calculations for the anatase crystal structure in a recent work⁷ to model the inelastic scattering of neutrons. Both have tetragonal symmetry but different elastic parameters. This results in different relative positions of the frequencies of the modes coming from a given isotropic mode.

Using the same measure as before, the frequency splitting for the S_2^1 modes is $\Delta=10\%$ and 20% for the anatase and rutile structure, respectively.

Due to the lowering of the symmetry compared to the cubic case, the breathing mode is also susceptible to more mixings. For anatase TiO_2 , the S_0^1 mode mixes mainly with T_5^1 (mode $i=67$), while for rutile TiO_2 it mixes mainly with S_2^2 (mode $i=41$).

C. Spherical nanocrystals with hexagonal crystallinity

As a last example of the influence of elastic anisotropy, we focus on nanospheres made of crystals having hexagonal symmetry, namely, CdSe (Table VI and Fig. 5 using the elastic constants from Ref. 27), Co (Table VII using the elastic constants from Ref. 28), and ZnO (elastic constants from

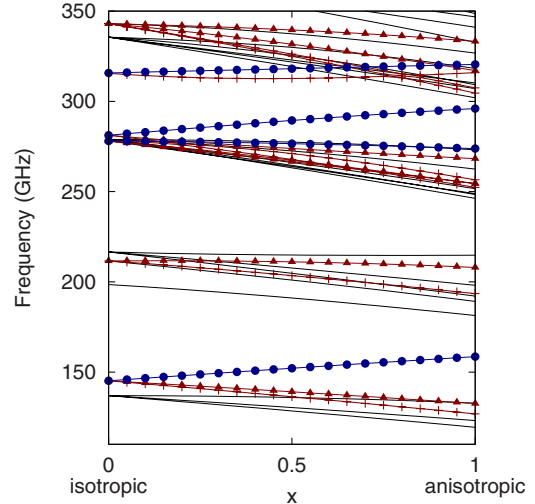


FIG. 5. (Color online) Evolution of the frequency of Raman-active modes of a monodomain wurtzite CdSe sphere (radius 5 nm) with varying elastic anisotropy up to the frequency range of the breathing mode. Raman-inactive modes are plotted with black lines, E_{1g} branches with lines and crosses (red online), E_{2g} branches with lines and triangles (red online), and A_{1g} branches with lines and full circles (blue online).

Ref. 18). The associated point group is D_{6h} . The most notable difference compared to previous symmetries is that some “accidental” degeneracy exists for such systems: for each $B_{1g}(B_{1u})$ vibration there is a $B_{2g}(B_{2u})$ vibration having the same frequency.

Using the same measure as before, the frequency splitting for the S_2^1 modes is $\Delta=9\%$, 11% , and 5% for the CdSe, Co, and ZnO, respectively. ZnO is therefore the most elastically isotropic among the materials studied in this work.

Regarding the breathing mode, for CdSe it is hardly mixed with other modes due to anisotropy and results in mode $i=77$ which has a strong projection onto S_0^1 and a large volume variation. For the nanosphere made of cobalt, there is a strong mixing with the S_2^2 and S_4^1 modes and the anisotropic mode with the largest projection onto S_0^1 and the largest volume variation is mode $i=49$ which is on the branch coming from S_4^1 at 466.7 GHz and not on the branch starting from S_0^1 at 536.8 GHz.

The infrared-active S_1^1 mode which was recently observed⁶ for CdSe nanoparticles is split by the lowering of symmetry into A_{2u} and E_{1u} modes at 181.9 and 181.3 GHz, respectively. This frequency splitting is very small but these modes mix with the branches having identical irreducible representations coming from S_3^1 . Neglecting this mixing, the isotropic S_1^1 is in excellent agreement with the anisotropic description.

D. Nonspherical nanocrystals

In order to illustrate the usefulness of the same numerical tools for a different source of anisotropy, we consider in the following the lowering of the symmetry due to the shape of the nanoparticles. We start with a minor change of the shape as the nanosphere is transformed into a spheroid having an

TABLE VIII. Characteristics of modes of a spheroid of dimensions $R=5$ nm, $R_z=10$ nm made from elastically isotropic (i.e., not monodomain) Ag. i is the mode index.

i	ν (GHz)	ir	δV
7–8	62.4	E_{1u}	0.0
9	71.1	A_{2u}	0.0
10	90.8	A_{1g}	0.4
11–12	103.8	E_{1g}	0.0
13	116.6	A_{2g}	0.0
14–15	127.0	E_{1g}	0.0
16–17	136.3	E_{2g}	0.0
...
34	185.2	A_{1g}	0.2
...
57	244.6	A_{1g}	1.0
...
64	253.3	A_{1g}	0.0
...
90	294.8	A_{1g}	4.5
...
110	318.8	A_{1g}	0.5
...

isotropic elasticity. Then we consider faceted nanoparticles with elastic anisotropy.

1. Spheroids with isotropic elasticity

Let us consider a spheroid made of silver with a degenerate semiaxis $R=5$ nm and a varying nondegenerate semiaxis R_z . We assume the elasticity to be isotropic. The point group associated with such a spheroid is therefore $D_{\infty h}$. The frequencies, irreducible representations, and volume variations

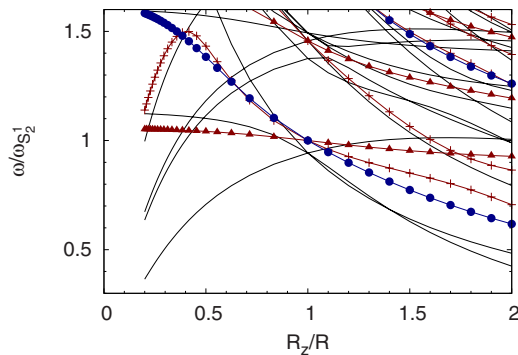


FIG. 6. (Color online) Reduced frequency of the vibrations of an elastically isotropic silver spheroid as a function of its aspect ratio. R is the length of the degenerate semiaxis and R_z is the length of the nondegenerate one. $\omega_{S_2^1}$ is the frequency of the S_2^1 mode of the sphere of radius R . Raman-inactive modes are plotted with black lines, E_{1g} branches with lines and crosses (red online), E_{2g} branches with lines and triangles (red online), and A_{1g} branches with lines and full circles (blue online).

for a spheroid with $R_z=10$ nm are presented in Table VIII. The branches obtained for varying R_z are presented in Fig. 6.

Let us now focus on the effect of the spheroidal deformation on the S_2^1 modes. Looking at the displacements corresponding to these modes for small deviations from the sphere, it is possible to understand the frequency variations. The lowest A_{1g} mode corresponds to a stretching along the z direction accompanied by a shrinking in the xy plane. Therefore it can be seen as a vibration confined along the z direction and its frequency varies roughly as $1/R_z$. The E_{2g} vibrations correspond to a stretching in the xy plane without changes along the z axis and therefore their frequencies hardly change with R_z . The E_{1g} vibrations correspond to a stretching in the xz and yz plane without changes along the z axis and therefore their frequencies vary with a slower eccentricity dependence than the previous mode. These rough approximations are in agreement with the dependence observed in Fig. 6.

Using perturbation theory,²⁹ it is possible to obtain more accurate expressions for the frequencies of these three branches. The exact variations for $|R_z-R|\ll R$ are $\Omega(1+4\beta/21)$, $\Omega(1-2\beta/21)$, and $\Omega(1-4\beta/21)$ for the E_{1g} , E_{2g} , and A_{1g} modes, respectively, where $\beta=2(R_z-R)/(R_z+R)$ and Ω is the frequency of modes S_2^1 for a spherical particle having the same volume. Note that the length of the degenerate semiaxis is constant in this work and therefore the volume varies linearly with R_z . Using $\Omega=\omega_{S_2^1}\sqrt[3]{R/R_z}$ results in expressions which are in very good agreement with Fig. 6 close to $R_z=R$.

Regarding the “breathing” mode, the picture gets very complicated when R_z/R differs significantly from 1. S_0^1 is on the fourth A_{1g} branch. Therefore the mode of the spheroid with $R_z/R=2$ on the same branch is mode $i=64$. However, due to the mixing with neighboring A_{1g} branches, the mode with $i=90$ is a better candidate since its volume variation is much larger. Thanks to this additional property of the symmetric modes, it is therefore possible to follow the breathing mode. However, because it is not possible to project onto the Lamb modes of an isotropic sphere due to the different shapes, only the branches and the anticrossing patterns between branches having the same irreducible representation can help tracking qualitatively the other S and T modes.

These calculations are targeted at interpreting experimental results on silver nanoparticles such as nanocolumns.³⁰ Compared to previous calculations using the FEMS method presented before,³¹ the current approach enables a more complete description of the different vibrations besides being faster and more accurate. In particular, the variation in volume is very efficient in showing which modes should be observed by time-resolved pump-probe experiments.⁴ It is interesting to note that some works^{4,30} concern aligned nanocolumns which results in interesting depolarization rules for the Raman peaks. For nonaligned nanoparticles, these rules are the same as those used routinely for an ensemble of molecules, i.e., all the Raman-active modes produce completely depolarized Raman peaks except for the A_{1g} vibrations which have a “polarized” scattering for which the Raman peak is more intense when the polarizations of the incident and scattered photons are parallel. For oriented nanoparticles, this rule does not hold and the angles of the incident and scat-

TABLE IX. Frequencies and irreducible representations of the lowest frequency vibrations of elastically anisotropic gold nanocrystals having different shapes. The volume of the different nanocrystals is the same as that of a sphere of radius 5 nm. The frequencies of the Raman-active modes (E_g and T_{2g}) are almost unaffected by the shape. See the text for the orientation of the crystal lattice with respect to the polyhedra.

ir	Sphere	Cuboctahedron	Truncated cuboctahedron
E_g	74.6	74.5	74.5
T_{2u}	76.9	73.4	75.5
A_{2g}	109.0	81.6	91.7
T_{1u}	111.2	108.7	110.7
E_u	114.1	102.3	107.9
T_{2g}	120.5	121.3	121.7
T_{2g}	140.2	128.0	133.8
...

tered photons with respect to the axis of symmetry of the nanoparticles have to be taken into account.

Recent time-resolved pump-probe femtosecond experiments for single gold nanoparticles³² also demonstrate the need for such a model. In particular, the observation of a peak close to the S_2^1 frequency is reported for spheroids but not for spheres. This is in agreement with the features reported here for silver, namely, that the A_{1g} mode coming from the S_2^1 mode has a nonzero volume variation enabling it to be observed in such an experiment unlike the S_2^1 mode of a sphere. It is also worth noting that the shape of the peak attributed to “the breathing mode” in this work for dumbbells looks quite complicated. Such nano-objects have the same symmetry as spheroids. As a result, in most cases there is no such thing as a breathing mode but rather a set of A_{1g} vibrations in a relatively narrow frequency range having a significant volume variation. This is due to the fact that the A_{1g} branch coming from the S_0^1 vibration mixes with all the other A_{1g} branches which come from all the S_ℓ vibrations with even ℓ . Modeling such gold dumbbells is beyond the scope of this paper but doing so would enable a more detailed understanding of the experimental results, especially for such single-particle measurements for which the external shape of the nanoparticles can be obtained from scanning electron microscopy (SEM) images. The relatively large size of these nanoparticles prevents them from being single domain and justifies the use of the isotropic elastic approximation.

2. Anisotropic gold polyhedra

Observation of faceted nanoparticles using electron microscopy is quite common. Such facets can be thought of as a signature of the inner crystal structure and therefore as an indication of the elastic anisotropy.³³ To quantify the importance of the shape on the vibrations, we calculated the frequencies and irreducible representations for some polyhedra and the results are presented in Table IX. The crystal lattice is oriented with respect to the shape so that the [100] planes correspond to the square faces for the cuboctahedron and to the octagonal faces for the truncated cuboctahedron. There is

no lowering of symmetry associated with these shapes compared to the case of a monodomain spherical gold nanoparticle. The relevant point group is then D_{4h} . While Table IX clearly shows that the lowest frequencies change with the shape, the frequencies of the lowest E_g and T_{2g} modes are hardly affected. Since the degeneracies of the S_0 and S_1 modes are not lifted, all the modes which are observable by Raman scattering, infrared absorption or time-resolved pump-probe experiments are not sensitive to these changes in shape.

IV. MULTIPLE-DOMAIN NANOPARTICLES

Several attempts have been made in the past either to fit low-frequency Raman spectra or to determine the size distribution of the nanoparticles inside a sample using the shape of the low-frequency Raman peak. Both approaches always rely on the validity of the isotropic model by Lamb and on the predominance of the size distribution, the coupling with a surrounding matrix and the electron-vibration coupling to fit the broadening of the peaks. However the distribution of internal structures of multiple-domain nanoparticles also results in inhomogeneous broadening.

It is in principle possible to model the vibrations of a multiple-domain nanoparticle using the numerical method of Visscher *et al.* However this requires a complete description of the position of the domain boundaries and the orientations of the crystal lattice. For ensemble measurements with the nanoparticles having a variety of different internal structure, a lot of calculations would be required. Otherwise, using such an approach for a single internal structure is justified only if all the studied nanoparticles are identical for ensemble measurements or if the inner structure of a nanoparticle studied in a single-particle measurement is perfectly known. Due to these latter two conditions having never been met until now and also to the additional complexity of modeling a multiple-domain nanoparticle, we suggest using the isotropic approximation to describe an ensemble of multiple-domain nanoparticles. What this means is that no nanoparticle behaves exactly as an isotropic nanoparticle, but the isotropic approximation gives an average value due to the nanoparticles having essentially random domain structures. Ensemble measurements should therefore show features associated with these average frequencies with some inhomogeneous width due to the inhomogeneous distribution of domains inside the population of nanoparticles.

We calculated the vibrations of an icosahedron made of gold and silver assuming the isotropic approximation to be valid in that case. The corresponding point group for such a nanoparticle is I_h . It is interesting to note that in this case there is no degeneracy lifting for the modes S_0 , S_1 , and S_2 whose irreducible representation in the new system is A_g , T_{1u} , and H_g , respectively. As a result, there is hardly any frequency difference compared to the case of a sphere having the same volume. A real icosahedron made of an anisotropic material but having the same symmetry due to the presence of twins would have no degeneracy lifting either for the same modes and we expect almost the same frequencies too.

V. CONCLUSION

We have presented mode frequencies and irreducible representations for homogeneous continuum nanoparticles using a standard numerical method which can handle arbitrary shape and anisotropic elasticity. The classification by irreducible representation makes it possible to label many modes as either Raman or infrared inactive. We have been able to go beyond this to provide some tools to make qualitative estimates of the Raman intensity of potentially Raman-active modes. These tools are well suited for the interpretation of experimental results obtained with vibrational spectroscopies.^{7,9}

This approach fills a large gap in current works since up to now it was necessary to choose between a simplified spherical isotropic model where the underlying physics was simple enough but where the accuracy was challenged by recent experimental results or a numerical approach which provides accurate frequencies but which is inefficient in practice due to the lack of tools to distinguish the relevant

vibrations without complex simulations of spectra.

It is clear that additional theoretical work is required in order to quantitatively predict Raman intensities for elastically anisotropic modes of spheres. However, the labeling of modes via their Lamb mode parentage by continuous variation of the elastic isotropy and projections for spherical nanoparticles is a powerful descriptive and semiquantitative tool for understanding what is going on with elastic anisotropy. The significant frequency splittings obtained in this work call into question the validity of the isotropic approximation for the case of multiple-domain nanoparticles. Such systems are very relevant experimentally but their vibrations remain largely unaddressed.

ACKNOWLEDGMENTS

L.S. acknowledges Eugène Duval for stimulating discussions and comments. D.B.M. acknowledges support from NSERC.

*lucien.saviot@u-bourgogne.fr

†daniel.murray@ubc.ca

¹E. Duval, A. Boukenter, and B. Champagnon, *Phys. Rev. Lett.* **56**, 2052 (1986).

²N. Del Fatti, C. Voisin, F. Chevy, F. Vallée, and C. Flytzanis, *J. Chem. Phys.* **110**, 11484 (1999).

³M. Ikezawa, J. Zhao, A. Kanno, and Y. Masumoto, *J. Phys. Soc. Jpn.* **74**, 3082 (2005).

⁴J. Burgin, P. Langot, A. Arbouet, J. Margueritat, J. Gonzalo, C. N. Afonso, F. Vallée, A. Mlayah, M. D. Rossell, and G. Van Tendeloo, *Nano Lett.* **8**, 1296 (2008).

⁵D. B. Murray, C. H. Netting, L. Saviot, C. Pighini, N. Millot, D. Aymes, and H.-L. Liu, *J. Nanoelectron. Optoelectron.* **1**, 92 (2006).

⁶T.-M. Liu *et al.*, *Appl. Phys. Lett.* **92**, 093122 (2008).

⁷L. Saviot, C. H. Netting, D. B. Murray, S. Rols, A. Mermet, A.-L. Papa, C. Pighini, D. Aymes, and N. Millot, *Phys. Rev. B* **78**, 245426 (2008).

⁸H. Lamb, *Proc. London Math. Soc.* **s1-13**, 189 (1881).

⁹H. Portalès, N. Goubet, L. Saviot, S. Adichtchev, D. B. Murray, A. Mermet, E. Duval, and M.-P. Piléni, *Proc. Natl. Acad. Sci. U.S.A.* **105**, 14784 (2008).

¹⁰W. M. Visscher, A. Migliori, T. M. Bell, and R. A. Reinert, *J. Acoust. Soc. Am.* **90**, 2154 (1991).

¹¹E. Duval, *Phys. Rev. B* **46**, 5795 (1992).

¹²S. Ino, *J. Phys. Soc. Jpn.* **27**, 941 (1969).

¹³P. R. Heyliger, E. Pan, S. Cook, and M. Manaloto, *J. Sound Vib.* **311**, 184 (2008).

¹⁴W. Cheng, S.-F. Ren, and P. Y. Yu, *Phys. Rev. B* **71**, 174305 (2005).

¹⁵W. Cheng, S.-F. Ren, and P. Y. Yu, *Phys. Rev. B* **72**, 059901(E) (2005).

¹⁶N. Combe, J. R. Huntzinger, and A. Mlayah, *Phys. Rev. B* **76**, 205425 (2007).

¹⁷F. Ramirez, P. R. Heyliger, A. K. Rappé, and R. G. Leisure, *J. Acoust. Soc. Am.* **123**, 709 (2008).

¹⁸N. Combe, P.-M. Chassaing, and F. Demangeot, *Phys. Rev. B* **79**, 045408 (2009).

¹⁹L. Saviot, D. B. Murray, and M. C. Marco de Lucas, *Phys. Rev. B* **69**, 113402 (2004).

²⁰D. B. Murray and L. Saviot, *Phys. Rev. B* **69**, 094305 (2004).

²¹A. N. Norris, *J. Mech. Mater. Struct.* **1**, 223 (2006).

²²Mass densities in g cm⁻³ and C_{ij} in GPa used in this work. Ag: $\rho=10.50$, isotropic $C_{11}=147.42$ and $C_{12}=83.84$; anisotropic $C_{11}=123.99$, $C_{12}=93.6$, and $C_{44}=46.12$. Au: $\rho=19.283$, isotropic $C_{11}=213.83$ and $C_{12}=153.57$; anisotropic $C_{11}=191$, $C_{12}=162$, and $C_{44}=42.4$. Si: $\rho=2.329$, anisotropic $C_{11}=166$, $C_{12}=63.9$, and $C_{44}=79.6$. Ge: $\rho=5.323$, anisotropic $C_{11}=126$, $C_{12}=44$, and $C_{44}=67.7$. Isotropic TiO₂: $\rho=3.9$, $C_{11}=303.72$, and $C_{12}=85.55$. Rutile TiO₂: $\rho=4.24$, anisotropic $C_{11}=268$, $C_{12}=175$, $C_{13}=147$, $C_{33}=484$, $C_{44}=124$, and $C_{66}=190$. Anatase TiO₂: $\rho=3.9$, anisotropic $C_{11}=320$, $C_{12}=151$, $C_{13}=143$, $C_{33}=190$, $C_{44}=54$, and $C_{66}=60$. CdSe: $\rho=5.81$, isotropic $C_{11}=74.05$ and $C_{12}=39.67$; anisotropic $C_{11}=74.6$, $C_{12}=46.1$, $C_{13}=39.4$, $C_{33}=81.7$, and $C_{44}=13$. Co: $\rho=8.836$, isotropic $C_{11}=323.42$ and $C_{12}=176.23$; anisotropic $C_{11}=307.1$, $C_{12}=165.0$, $C_{13}=102.7$, $C_{33}=358.1$, and $C_{44}=75.5$. ZnO: $\rho=5.676$, anisotropic $C_{11}=209.7$, $C_{12}=121.1$, $C_{13}=105.1$, $C_{33}=210.9$, and $C_{44}=42.47$.

²³J. R. Neighbours and G. A. Alers, *Phys. Rev.* **111**, 707 (1958).

²⁴R. F. S. Hearmon, in *The Elastic Constants of Crystals and Other Anisotropic Materials*, Landolt-Börnstein New-Series Group III Vol. 18, edited by K. H. Hellwege and A. M. Hellwege (Springer-Verlag, Berlin, 1984).

²⁵G. Bachelier and A. Mlayah, *Phys. Rev. B* **69**, 205408 (2004).

²⁶M. Iuga, G. Steinle-Neumann, and J. Meinhardt, *Eur. Phys. J. B* **58**, 127 (2007).

²⁷E. Rabani, *J. Chem. Phys.* **116**, 258 (2002).

²⁸P. Gangopadhyay, T. R. Ravindran, K. G. M. Nair, S. Kalavathi, B. Sundaravel, and B. K. Panigrahi, *Appl. Phys. Lett.* **90**, 063108 (2007).

²⁹G. Mariotto, M. Montagna, G. Viliani, E. Duval, S. Lefrant, E.

- Rzepka, and C. Mai, *Europhys. Lett.* **6**, 239 (1988).
- ³⁰J. Margueritat, J. Gonzalo, C. N. Afonso, A. Mlayah, D. B. Murray, and L. Saviot, *Nano Lett.* **6**, 2037 (2006).
- ³¹D. B. Murray, A. S. Laarakker, and L. Saviot, *Phys. Status Solidi C* **3**, 3935 (2006).
- ³²A. L. Tchegotareva, M. A. van Dijk, P. V. Ruijgrok, V. Fokkema, M. H. S. Hesselberth, M. Lippitz, and M. Orrit, *ChemPhysChem* **10**, 111 (2009).
- ³³B. Stephanidis, S. Adichtchev, S. Etienne, S. Migot, E. Duval, and A. Mermet, *Phys. Rev. B* **76**, 121404(R) (2007).